

OPTICS

Nonlinearity symmetry breaking for generating tunable quantum entanglement in semiconductor metasurfaces

Jinyong Ma^{1*†‡}, Tongmiao Fan^{1†}, Tuomas Haggren^{1†}, Laura Valencia Molina^{1,2}, Matthew Parry¹, Saniya Shinde^{2,1}, Caitlin McManus-Barrett¹, Jihua Zhang^{1,3}, Rocio Camacho Morales¹, Frank Setzpfandt^{2,4}, Hark Hoe Tan¹, Chennupati Jagadish¹, Dragomir N. Neshev¹, Andrey A. Sukhorukov^{1*}

Tunable biphoton quantum entanglement generated from nonlinear flat optics is highly desirable for cutting-edge quantum technologies, yet its tunability is substantially constrained by the symmetry of material nonlinear tensors. Here, we overcome this constraint by introducing symmetry breaking in nonlinear polarization via resonant metasurfaces. While asymmetric optical responses have enabled breakthroughs in classical applications like nonreciprocal light transmission, we report the experimental demonstration of asymmetric nonlinear responses for biphoton entanglement. Using a structural-asymmetric semiconductor metasurface incorporating [110] InGaP nanoresonators, we realize continuous tuning of polarization entanglement from partially entangled states to a Bell state by adjusting the pump wavelength. We also observe pronounced spatial anti-correlations and theoretically confirm that this approach can extend to tailor hyperentanglement. Furthermore, our nanoscale entanglement source features an ultrahigh coincidence-to-accidental ratio of $\approx 7 \times 10^4$, outperforming existing semiconductor flat optics by two orders of magnitude. Introducing asymmetric nonlinear response in quantum metasurfaces opens directions for tailoring on-demand quantum states.

INTRODUCTION

Tunable photonic quantum entanglement promises to advance information processing beyond classical approaches, facilitating applications in quantum communications (1), imaging (2), and computing (3). A practical approach to preparing quantum entanglement at room temperature is to engineer photon-pair generation through spontaneous parametric down-conversion (SPDC). Linear metasurfaces, composed of subwavelength-thick nanostructures, have recently been introduced in quantum optics to manipulate and transform the biphoton quantum states generated from bulky nonlinear crystals, showing a novel approach for integrated quantum devices (4, 5). To push the boundary of ultracompactness, flat-optics devices incorporating nonlinear materials are emerging as new platforms for generating photon pairs at the nanoscale (6–10). In particular, nanostructured metasurfaces supporting optical resonances can enhance and tailor SPDC processes, allowing for the generation of spectral (10), polarization (11–13), and spatial (14, 15) entanglement. However, the tunability of polarization entanglement (16) is generally subject to the symmetry of nonlinear tensors of materials, including dielectric materials (11), III-V semiconductors (17), or van der Waals materials (18–21), where the pump photon polarization serves as the only tuning parameter. As a result, achieving entanglement with comprehensive, real-time, and ultrafast tunability, which is critical for quantum information processing (22, 23), remained a major challenge (24).

Optical systems with asymmetric responses are fundamental to optical information processing (25–28), allowing extensive manipulation of light propagation. Recent developments of flat optics open up new opportunities in this direction (6). For example, flat optics with electromagnetic nonlinearities have enabled optical nonreciprocity (29, 30), offering unique benefits like the absence of external bias and ultracompactness at the subwavelength scale. Asymmetric nonlinear frequency conversion (31–33) in metasurfaces and tunable nonlinear tensor in twisted two-dimensional materials (34) were also recently realized in experiments. However, the implications of asymmetric response have been limited to the classical regime in flat optics. While various quantum phenomena arising from asymmetric response have recently received substantial attention in other platforms such as optomechanical (35, 36) or atomic systems (37–41), introducing asymmetric responses to tailor SPDC processes remained experimentally unexplored in any nonlinear systems.

Here, we propose and experimentally demonstrate a unique mechanism, through the control of asymmetric nonlinear response, for generating optically tunable biphoton quantum entanglement, overcoming the tunability limit set by material nonlinear tensors. We develop a resonant semiconductor metasurface incorporating [110] InGaP nanostructures, where structural asymmetry breaks the rotational symmetry of the nonlinear polarization. The degree of symmetry breaking is controlled via the biphoton wavelength, allowing dynamic manipulation of asymmetric second harmonic generation (SHG). Leveraging this unique characteristic, we realize continuous tuning of polarization-entangled states in a wide range, from a partially entangled state to a Bell state via the pump wavelength, which is unattainable in unpatterned materials. Additionally, we experimentally detect pronounced spatial anti-correlations of photon pairs and theoretically show that this unique mechanism can extend to produce optically tunable hyperentanglement in the polarization and spatial degrees of freedom. Introducing asymmetric nonlinear response in quantum metasurfaces opens directions for tailoring on-demand quantum states and beyond.

¹ARC Centre of Excellence for Transformative Meta-Optical Systems (TMOS), Department of Electronic Materials Engineering, Research School of Physics, The Australian National University, Canberra, ACT 2601, Australia. ²Abbe Center of Photonics, Friedrich Schiller University Jena, Jena, Germany. ³Songshan Lake Materials Laboratory, Dongguan 523808, P. R. China. ⁴Fraunhofer Institute for Applied Optics and Precision Engineering IOF, Jena, Germany.

*Corresponding author. Email: jinyong.ma@szu.edu.cn (J.M.); andrey.sukhorukov@anu.edu.au (A.A.S.)

†These authors contributed equally to this work.

‡Present address: Institute of Quantum Precision Measurement, State Key Laboratory of Radio Frequency Heterogeneous Integration, College of Physics and Optoelectronic Engineering, Shenzhen University, Shenzhen 518060, P.R. China.

Furthermore, the InGaP metasurface platform introduced here is a leading candidate for next-generation ultracompact quantum light sources, featuring a large second-order susceptibility χ_{xyz} of 220 pm/V (42), a wide bandgap of ~ 650 nm, and a high crystal quality due to lattice matching to GaAs substrate in epitaxial growth. Consequently, the measured SPDC rate and coincidence-to-accidental ratio (CAR) are record high at the infrared telecommunication wavelength in flat-optics photon-pair sources. The achieved CAR of $\approx 7 \times 10^4$ exceeds those reported in other semiconductor flat optics by two orders of magnitude (9, 10, 17–19, 43). This ultracompact and low-noise metasurface-based photon-pair source with optically tunable quantum entanglement is well suited for future monolithic integration with III-V semiconductor lasers, modulators, and detectors (44), offering unprecedented opportunities for quantum technologies.

RESULTS

Concept and modeling

We develop a nonlinear metasurface based on the InGaP platform (see Fig. 1A), which allows for the monolithic integration of various optical components (like lasers, modulators, and detectors) (44, 45)

on a single chip, opening opportunities for next-generation ultracompact quantum light sources with unique functionalities.

The dimensions of the metasurface are shown in Fig. 1B, where each meta-atom incorporates a 500-nm-thick InGaP nanopillar filled with an interlayer of SU-8-2. The tilting angle of 6° due to the etching process is considered in the simulation. The detailed metasurface design and rationale are provided in section S1.3. The InGaP nanostructures feature a [110] crystal orientation, providing a specific nonlinear polarization along the x direction, i.e., $P_x = 4\epsilon_0 d_{36}(E_{xs}E_{yi} + E_{ys}E_{xi})$ (section S1). Here, $d_{36} = \frac{1}{2}\chi_{xyz}$ is the effective nonlinear coefficient and ϵ_0 is the vacuum permittivity. The subscripts of the electric field E denote direction with x, y and signal/idler photons with s, i . This inherently enables the generation of cross-polarized photon pairs under an x -polarized pump, showing a symmetry between $E_{xs}E_{yi}$ and $E_{ys}E_{xi}$ processes.

We consider counterpropagating SPDC sketched in Fig. 1A, which naturally splits the signal and idler photons and allows unique entanglement tunability. The polarization of signal/idler photons is in a quantum superposition of $|H_s V_i\rangle$ and $|V_s H_i\rangle$ (where V and H represent x and y directions). To ensure quantum coherence, a high spatial overlap between $|H_s V_i\rangle$ and $|V_s H_i\rangle$ is a prerequisite. This is

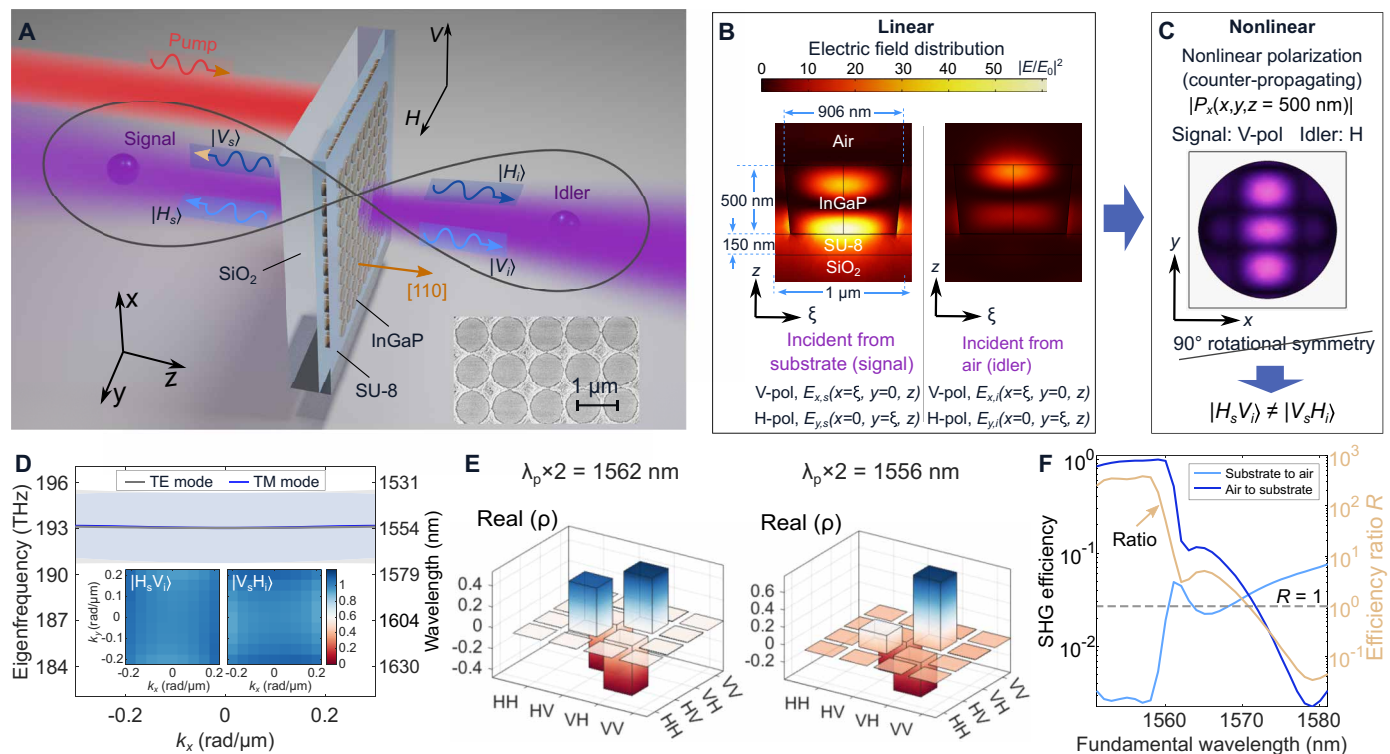


Fig. 1. Generation of optically tunable polarization entanglement in an InGaP metasurface. (A) Sketch of polarization entanglement from an InGaP metasurface. The nanostructured [110] InGaP metasurface enables enhanced generation of polarization-entangled photon pairs counterpropagating along the z direction. The bottom right panel presents the scanning electron microscope image of the fabricated metasurface. (B) and (C) Profiles of optical resonances and nonlinear polarization in the metasurface. Due to the structural asymmetry of the metasurface along the z direction, the electric field distributes differently as the beam is incident from the substrate (signal arm) or air side (idler arm) of the metasurface (B). This breaks the 90° symmetry of the nonlinear polarization (C), leading to different nonlinear processes for $|H_s V_i\rangle$ and $|V_s H_i\rangle$. The origin is located at the center of the InGaP nanopillar's bottom surface. (D) Simulated eigenfrequency of optical resonances versus transverse wavenumber k_x . The eigenfrequencies of the TE and TM modes supported by the metasurface manifest a flat band within the linewidth of optical resonances due to the localized nature of the modes. As a result, the emission patterns of SPDC processes $|H_s V_i\rangle$ (left inset) and $|V_s H_i\rangle$ (right inset) are close to flat in the k space, ensuring their spatial overlaps. (E) Simulated density matrices at different pump wavelengths. At $\lambda_p \times 2 = 1562$ nm, a polarization Bell state can be produced with a high fidelity of 98% and a concurrence of 0.99. A different polarization-entangled state is produced as the pump wavelength is changed to $\lambda_p \times 2 = 1556$ nm. (F) Asymmetric SHG. Two SHG processes are simulated: excitation from the substrate (or air) and collection from the air (or substrate). Their efficiency ratio of $R = 1$ corresponds to fully symmetric SHG.

achieved by tailoring metasurface optical resonances to be localized (see Fig. 1B), where the resonance wavelengths (≈ 1554 nm) for transverse electric (TE) and transverse magnetic (TM) modes form nearly a flat band within their linewidths across a large range in k space (see Fig. 1D). The flat band is enabled by the high refractive index ~ 3.12 (42) of InGaP. Consequently, the simulated biphoton spatial emission rate for both $|H_s V_i\rangle$ and $|V_s H_i\rangle$ processes is flat and manifests high overlap in k space (see insets), enabling high-quality polarization entanglement. As shown in Fig. 1E, the simulated density matrix reveals an entangled polarization Bell state $|\Psi^-\rangle = \frac{1}{\sqrt{2}}(|H_s V_i\rangle - |V_s H_i\rangle)$ at the pump wavelength $\lambda_p \times 2 = 1562$ nm, with a fidelity of $>98\%$ and a concurrence of >0.99 . The minus sign in $|\Psi^-\rangle$ is caused by a π phase difference in counterpropagating SPDC processes. Notably, a differently polarization-entangled state is generated at a different pump wavelength $\lambda_p \times 2 = 1556$ nm. The control of polarization entanglement is enabled by a unique tuning mechanism—the symmetry breaking of the nonlinear polarization within the nanostructures. While the metasurface design itself is not unique, we emphasize that the nonlinear symmetry breaking is introduced to the SPDC for the first time.

To understand this mechanism, we analyze classical nonlinear processes SHG and sum frequency generation (SFG), which also reveal information about SPDC. Figure 1B reveals that co-polarized signal/idler photons incident from the substrate or air manifest different electric field distributions inside the InGaP in the x - y plane for a given z , i.e., $E_{x,s}^{(V_s)}(x, y) \neq E_{x,i}^{(V_i)}(x, y)$ and $E_{x,s}^{(H_s)}(x, y) \neq E_{x,i}^{(H_i)}(x, y)$, where the superscripts represent the photon polarization. This characteristic is caused by the geometric asymmetry of the sample including the metasurface and a substrate in the z direction. As a result, the SHG manifests an asymmetric response (31, 33) controllable via the fundamental wavelength (see Fig. 1F). We note that this result is to establish a connection to previous studies on the diode-like asymmetric SHG process (31, 33), where the signal and idler photons are co-propagating. The result does not directly correspond to the observations for the counterpropagating configuration primarily considered in this work. As compared to the co-propagating case, the nonlinear polarization for counterpropagating signal/idler photons breaks the 90° rotational symmetry in the x - y plane (see Fig. 1C), leading to asymmetric SFG processes for $P_x^{(V_s H_i)}(x, y)$ and $P_x^{(H_s V_i)}(x, y)$. Due to the classical-to-quantum correspondence (46, 47), the quantum efficiency of $|H_s V_i\rangle$ and $|V_s H_i\rangle$ processes can also differ. As the pump frequency changes, the signal and idler wavelengths vary along with their respective mode profiles within the nanostructures. This alters the symmetry of the corresponding nonlinear polarization and thus the tuning of polarization entanglement. Note that such tunability induced by symmetry breaking is not applicable for co-propagating SPDC in the present metasurface, due to the C_{4v} symmetry of the nanostructures. We clarify that Fig. 1C displays only the nonlinear polarization profile for $P_x^{(V_s H_i)}(x, y)$, while the profile for $P_x^{(H_s V_i)}(x, y)$ can be obtained by rotating $P_x^{(V_s H_i)}(x, y)$ by 90° . In section S2, we provide the profiles for both cases and present a comprehensive and quantitative explanation of how symmetry breaking leads to asymmetric SPDC.

Experimental characterization of enhanced nonlinear processes

We first experimentally measure the angle-dependent linear transmission of the metasurface (see Fig. 2A). Optical resonances are signified by transmission minima for H- and V-polarized inputs and

overlap at ≈ 1550 nm with $Q \approx 25$ and $Q \approx 30$, respectively, showing reasonable agreement with the designed metasurface shown in Fig. 1D. Both modes manifest a flat band across a large incident angle range of $\pm 10^\circ$. To understand the optical enhancement and nonlinear tensor, we characterize the V-polarized SHG from the InGaP metasurface, as shown in Fig. 2 (B and C). The SHG is enhanced 50 times at the resonance wavelength compared to the off-resonance excitation. The SHG efficiency is maximized for a diagonal or anti-diagonal polarized fundamental beam, confirming the presence of the nonlinear tensor component P_x .

We proceed with SPDC characterization using the experimental setup shown in Fig. 2D, where detailed procedures are provided in section S4. With the same collection angle of 3° , the measured coincidence rates of the photon pairs from the metasurface and unstructured InGaP film are compared in Fig. 2E, revealing a 25-fold SPDC enhancement due to the optical resonances supported by the metasurface. We also find that the measured SPDC rate depends linearly on the pump power (see Fig. 2F). Linear fitting to experimental data yields a detected SPDC rate of 0.1 Hz/mW, which is record high for flat optics quantum light sources at the infrared telecommunication wavelengths (see section S5). This high rate is attributed to the large second-order nonlinear coefficient, the use of [110] crystal orientation, and flat biphoton emission.

We present the CAR of biphoton emission from the metasurface at different pump powers in Fig. 2G. The solid curve is obtained from linear fitting of the SPDC rate and single-photon count rates (section S5). The decrease in CAR at pump powers < 5 mW is due to dark counts. Notably, the maximum CAR value reaches $\approx 7 \times 10^4$, which is record higher than in any existing photon-pair source with flat optics (see the benchmarking in section S5). This CAR exceeds those reported in previous works on semiconductor flat optics by two orders of magnitude, including two-dimensional materials (9, 18) and other III-V semiconductors (10, 17). The CAR also exceeds those in metasurfaces (14, 48) incorporating dielectric material traditionally used for SPDC and epsilon-near-zero metasurfaces (12). We attribute the high CAR achieved with InGaP metasurfaces to several key factors: a wide bandgap at 1.9 eV (~ 650 nm), high-crystal qualities due to lattice matching to GaAs substrate in epitaxial growth, high second-order nonlinearity of 220 pm/V (42), and optical resonances supported by the metasurface. As compared to existing flat-optics platforms (see section S5), we find that only the (110) InGaP metasurface has all these features, which results in the highest CAR reported in these platforms. For example, the second-order nonlinear coefficient of LiNbO₃ is about 10 times lower than that of InGaP, despite its larger bandgap and high crystal quality. We note that the fluorescence produced from the bandgap remains negligible as long as the pump photon energy is smaller than the bandgap energy. Since the highest CAR reported here is limited by the dark counts of the detectors and environment, we anticipate that the CAR can be further improved by replacing the avalanche photodiode detectors used in this work with superconducting nanowire single-photon detectors that offer lower dark counts. With such ultralow noise, the SPDC rate can be substantially increased by enhancing pump power through additional optical resonance at the pump wavelength while maintaining a high CAR. These results suggest that the InGaP metasurface platform is highly attractive for future SPDC-based quantum technologies.

We analyze the polarization properties of the generated photon pairs by varying the idler half-wave plate (HWP) angle $\theta_{H,i}$ for three

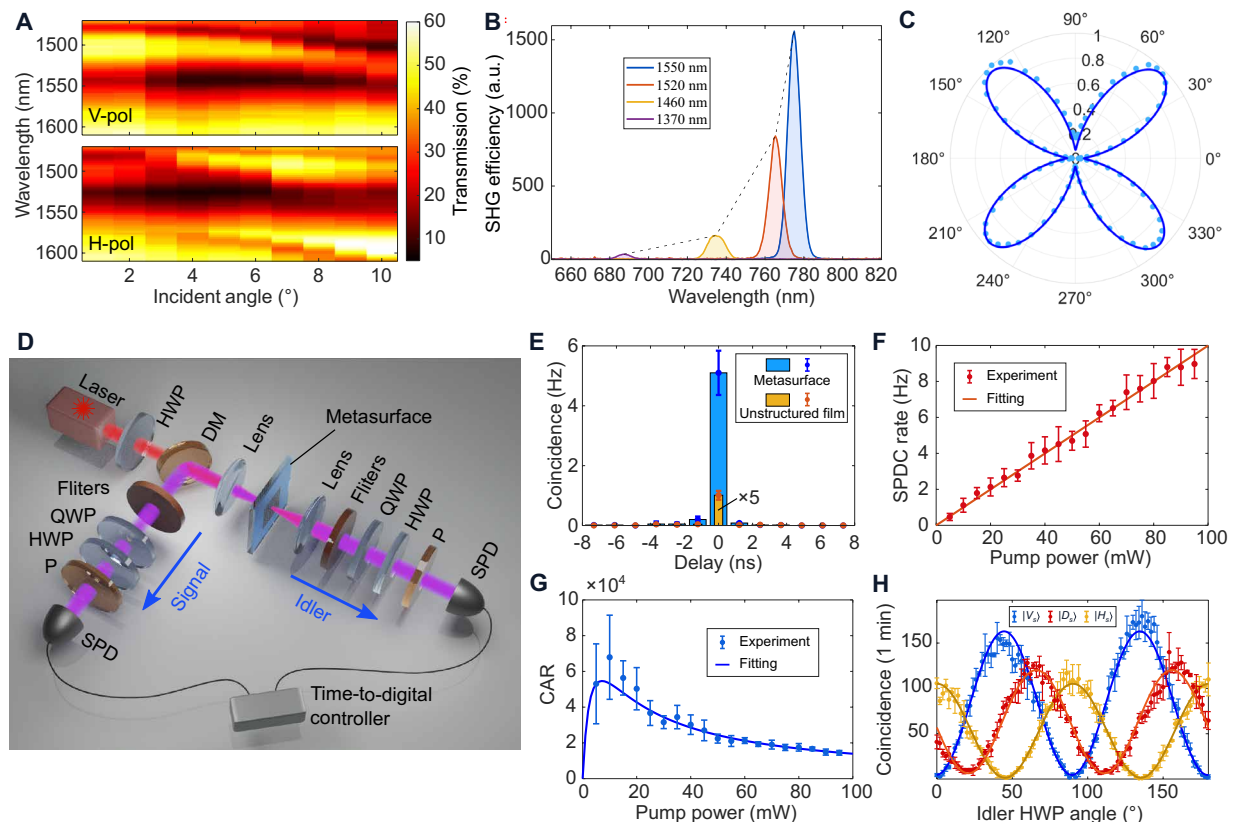


Fig. 2. Experimental characterization of nonlinear processes. (A) Measured linear transmission spectra versus incident angle for V- and H-polarized beams. The fabricated metasurface manifests optical resonances at ~ 1550 nm with a flat band for both polarizations. (B) Enhanced generation of SHG. The SHG efficiency is enhanced by 50 times at the resonance wavelength (blue curve) as compared to off-resonance excitation (purple curve). Maxima is connected by a dashed line for clarity. (C) SHG efficiency versus polarization of the fundamental beam. The SHG efficiency is maximized at D-polarized fundamental beam, attributed to the nonlinear tensor of InGaP [110]. (D) Experimental setup for characterizing SPDC. The backpropagating signal photons reflected by the dichroic mirror (DM) and the forward-propagating idler photons go through a set of optical filters, after which their polarizations are analyzed with a half-wave plate (HWP), a quarter-wave plate (QWP), and a polarizer (P). (E) Coincidence histograms for metasurface and unstructured thin film. The measured photon-pair rate from the metasurface reveals a 25-time enhancement compared to that from the unstructured thin film. (F) SPDC rate versus pump power. The measured SPDC rate linearly depends on the pump power. (G) CAR versus pump power. The correlation measurement manifests extremely high CAR values, reaching a maximum of $\approx 7 \times 10^4$. (H) Coincidence counts versus HWP plate angle at idler arm $\theta_{H,i}$. We fix polarization projections of signal photons to $|V_s\rangle$, $|D_s\rangle$, and $|H_s\rangle$. The visibility for these three cases is $>89\%$, violating the Bell inequality and confirming the presence of entanglement. Error bars indicate one SD in all plots.

signal polarization projections $|V_s\rangle$, $|D_s\rangle$, and $|H_s\rangle$. Figure 2H shows periodic oscillations in all three cases. The smallest visibility is $v = 89 \pm 2\%$ for the $|D_s\rangle$ projection, which is larger than 71%. This violates the Bell inequality by 9 SD, confirming the generation of polarization entanglement (49, 50).

Experimental confirmation of optically tunable polarization entanglement

Next, we experimentally perform full quantum tomography and reconstruct density matrices using the maximum likelihood method (51). All following measurements shown in Fig. 3A are performed using a V-polarized pump, with results for an H-polarized pump provided in section S6. At $\lambda_p \times 2 = 1558$ nm, the reconstructed density matrix reveals a polarized Bell state $|\Psi^-\rangle = \frac{1}{\sqrt{2}}(|H_s V_i\rangle - |V_s H_i\rangle)$ with fidelity of 95% and concurrence of 0.9. Most importantly, the polarization entanglement can be tuned by varying the pump wavelength. For example, at $\lambda_p \times 2 = 1574$ nm, the $|V_s H_i\rangle$ projection becomes more dominant over $|H_s V_i\rangle$.

To explore such tunability further, we measure the SPDC rate under $|V_s H_i\rangle$ and $|H_s V_i\rangle$ projections versus $\lambda_p \times 2$ as shown in Fig. 3B, where the unevenly spaced wavelengths are due to laser diode mode hopping. We observe differing wavelength dependence in measured coincidences for $|V_s H_i\rangle$ and $|H_s V_i\rangle$, indicating that each pump wavelength corresponds to a different polarization-entangled state ρ with distinct diagonal coefficients $\alpha = \langle H_s V_i | \rho | H_s V_i \rangle$ and $\beta = \langle V_s H_i | \rho | V_s H_i \rangle$. The measured coincidence rates of $|H_s V_i\rangle$ and $|V_s H_i\rangle$ are proportional to coefficients α and β , respectively, with their ratio α/β shown in Fig. 3C. The ratio can be controlled from 0.1 (a partially entangled state) to 0.8 (approaching a maximally entangled Bell state) by simply changing λ_p ; meanwhile, the SPDC rate is enhanced as compared to unpatterned thin films across these pump wavelengths. Furthermore, we characterize the concurrence and purity of the reconstructed quantum states (see Fig. 3D). The concurrence decreases at longer pump wavelengths from ~ 0.9 to ~ 0.7 because the quantum state changes from a Bell state to a less entangled state. However, the state purity remains above ~ 0.8 for all pump wavelengths, suggesting that all

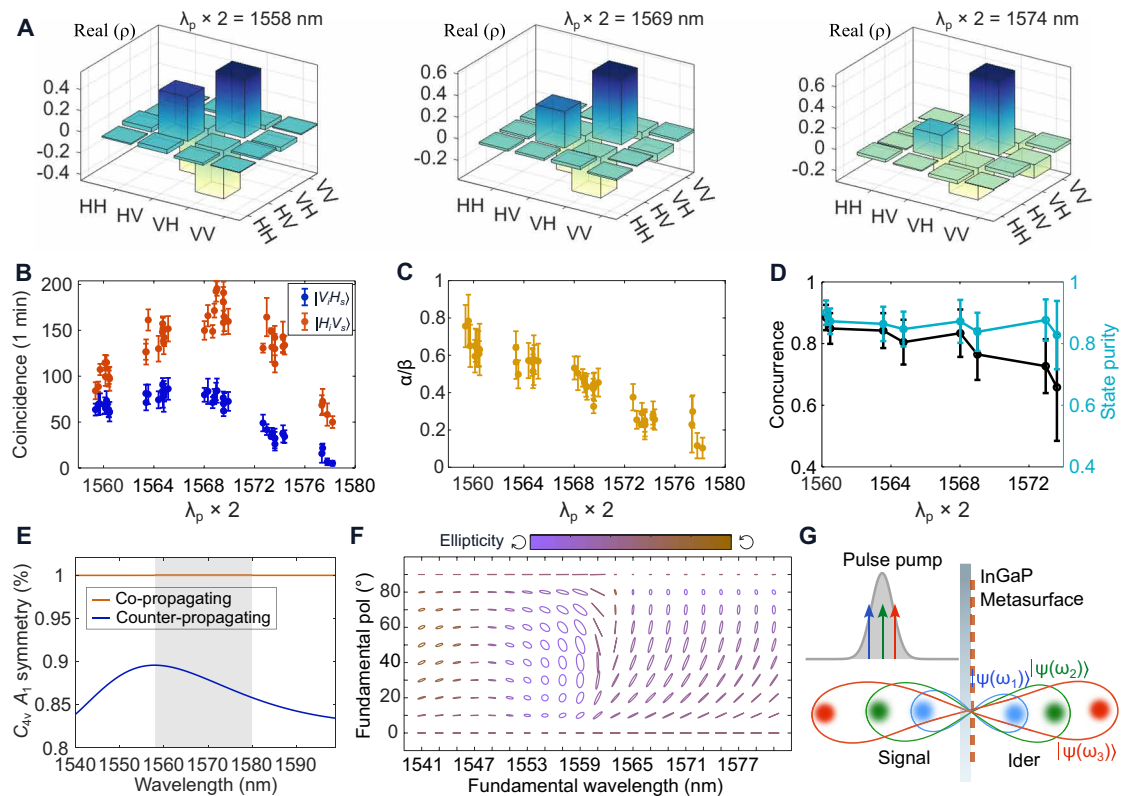


Fig. 3. Experimental characterization of optically tunable polarization entanglement. (A) Reconstructed density matrix at pump wavelength $\lambda_p \times 2 = 1558$ nm. The density matrix presents polarization entanglement close to a fully entangled Bell state $|\Psi^-\rangle = \frac{1}{\sqrt{2}}(|H_iV_i\rangle - |V_iH_i\rangle)$, with fidelity $>95\%$ and concurrence >0.9 . The density matrix changes at different pump wavelengths $\lambda_p \times 2 = 1569$ nm or 1574 nm. (B) Measured photon-pair rates versus pump wavelength. The biphoton coincidences measured at polarization projections $|H_iV_i\rangle$ and $|V_iH_i\rangle$, respectively, show distinct dependence over pump wavelengths. (C) Coefficient α/β of polarization-entangled state versus pump wavelength. The coefficient α/β calibrated from (C) is optically tunable by changing the pump wavelength. (D) Concurrence and state purity versus pump wavelength. The concurrence drops as the pump wavelength is tuned, while the state purity remains high. (E) Symmetry analysis of the nonlinear polarization by projecting its field onto the A_1 symmetry of the C_{4v} point group. The degree of symmetry breaking enables the tuning of the state coefficients. The shaded region represents the range of $\lambda_p \times 2$ used in (C) and (D). (F) Simulated polarization of counterpropagating SHG versus the fundamental wavelength and polarization, indicating extensive tunability of entanglement. Each ellipse represents the SHG polarization state in phase space, with its size indicating the SHG efficiency and its color suggesting ellipticity. (G) Perspective with a pulse-shaped pump. Pumping the metasurface with a shaped pulse allows ultrafast tuning of polarization entanglement, enabling high-speed information encoding. Error bars indicate one SD in all plots.

entangled states produced here are indeed in a coherent superposition of $|H_iV_i\rangle$ and $|V_iH_i\rangle$.

To provide a physical insight into the measurement results, we perform a quantitative symmetry analysis (52) of the nonlinear polarization by projecting its distribution onto the irreducible representations of the C_{4v} point group. We consider 20 x - y planes equally distributed along the z axis within the nanostructures and analyze the overall symmetry across each plane weighted by the average amplitude of the in-plane nonlinear polarization. The A_1 symmetry parameter η versus pump wavelength, indicating the degree of symmetry (ranging from 0 to 1), is shown in Fig. 3E (see detailed analysis in section S2). In the co-propagating nonlinear process, the nonlinear polarization maintains a high degree of symmetry ($\eta \sim 1$) across all wavelengths. However, for the counterpropagating case, the dependence of η on the pump wavelength correlates with changes in quantum states. At $\alpha/\beta \approx 1$, η tends to be maximized, suggesting the largest symmetry. The ratio α/β decreases or increases as η becomes smaller, thereby breaking the symmetry of nonlinear polarization.

This is a manifestation of an asymmetric nonlinear response in a quantum metasurface.

Furthermore, a more comprehensive entanglement tunability can be achieved by including pump polarization as an additional tuning parameter. The simulated SHG for counterpropagating signal/idler, presented in Fig. 3F, shows that fundamental wavelength and polarization provide extensive control over SHG polarization. The use of different optical modes also reveals the control in distinct regimes (section S7). These findings indicate a notable potential to broadly extend the range of entanglement tunability. While comprehensive tuning of the pump polarization is generally limited to the nanosecond scale (24, 53), its combination with wavelength-enabled ultrafast tuning may facilitate dynamic tuning of on-demand quantum states unattainable with unstructured nonlinear crystals.

This unique tunability can potentially stimulate a wide range of applications with a pulse-shaped pump (see Fig. 3G) whose Fourier transform presents a frequency comb (54–56). Each tooth of the comb carries one pump frequency for generating a unique polarization-entangled

state at the corresponding biphoton wavelength. A direct application is multiplexing polarization entanglement into each wavelength channel (57, 58), allowing the distribution of quantum states to multiple users. A key benefit of our approach is that the entanglement can be tailored in each channel for data transmission to different users. Additionally, time-division multiplexing can be achieved by allowing one photon to travel through a dispersive medium such that its travel time varies depending on its wavelength, while the other photon propagates through free space. As a result, each entangled state is encoded into different time bins at picosecond resolution according to its wavelength, enabling ultrafast switching of polarization entanglement. These multiplexing schemes may allow multi-user networks (22, 57, 58), and the ultrafast switching may be suited for routers compatible with existing high-speed telecommunication infrastructure (59). Furthermore, this tuning approach may enable the generation of tunable multiphoton states. For example, we consider two independent biphoton entanglements generated from two teeth of the frequency comb, $|\psi_1\rangle = a_1 |H_{s,1} V_{s,1}\rangle + b_1 |V_{s,1} H_{s,1}\rangle$ and $|\psi_2\rangle = a_2 |H_{s,2} V_{s,2}\rangle + b_2 |V_{s,2} H_{s,2}\rangle$. By post-selecting four-photon events (54), the generated state becomes $|\Psi\rangle = |\psi_1\rangle \otimes |\psi_2\rangle = a_1 a_2 |H_{s,1} V_{s,1} H_{s,2} V_{s,2}\rangle + a_1 b_2 |H_{s,1} V_{s,1} V_{s,2} H_{s,2}\rangle + b_1 a_2 |V_{s,1} H_{s,1} H_{s,2} V_{s,2}\rangle + a_2 b_2 |V_{s,1} H_{s,1} V_{s,2} H_{s,2}\rangle$, where the state coefficients can be controlled via pump wavelength and polarization. In these applications, our approach allows real-time tuning and is scalable depending on the number of teeth in the pump frequency comb.

We note that the biphoton wavelength remains stable once the tuning is set, although this tuning mechanism shifts the biphoton wavelength. Previous works (60, 61) have demonstrated that pulsed pump beams carrying a frequency comb enable wavelength-multiplexed quantum networks, where biphoton frequency bins allow for quantum information encoding and the photon spectrum is not fixed. These experiments reveal the practical feasibility of ultrafast tuning of polarization entanglement via a pump frequency comb proposed in our work (see Fig. 3G), which may naturally be incorporated in wavelength-multiplexed quantum networks.

Experimental characterization of spatial correlations and perspective in tunable hyperentanglement

This unique tuning mechanism can be extended to control photon pairs hyperentangled in more than one degree of freedom, which can bring exciting possibilities to future quantum technologies. We first calibrate the spatial correlations of signal and idler photons in addition to their polarization, using the setup illustrated in Fig. 4A. We remove all waveplates and polarizers and add a square aperture with width L in the Fourier plane (k space) for both signal and idler arms. At $k_{ap,s} = 0$ (see Fig. 4B), coincidences measured against $k_{ap,i}$ provide spatial information about photon-pair emission and collection (see section S8). Figure 4 (C and D) presents spatial correlation measurements at $k_{ap,s} = -L/2$ and $L/2$. Almost no photon pairs are detected when $k_{ap,s} = k_{ap,i} = -L/2$ or $L/2$; meanwhile, maximum coincidences occur at $k_{ap,s} = -k_{ap,i} = L/2$ and $-L/2$. These observations prove pronounced spatial anti-correlation of photon pairs in k space with opposite transverse momenta. Additionally, the simultaneous presence of $k_{ap,s} = L/2$, $k_{ap,i} = -L/2$ and $k_{ap,s} = -L/2$, $k_{ap,i} = L/2$ indicates the superposition of two spatial quantum states and spatial entanglement. The complete characterization of entanglement requires additional measurements at different spatial projections (62), which goes beyond the scope of this work but presents an interesting

avenue for future studies. Note that the polarization entanglement is reconstructed by summing over all spatial modes and spatial correlations are measured without polarization projections, suggesting the presence of a hyperentangled state being a product state of polarization and spatial states.

Inspired by the experiment, we theoretically confirm the generation of hyperentanglement from the metasurface (see Fig. 4E). As a proof of principle, we analyze the spatial entanglement $|\Psi_{\text{spatial}}\rangle = \frac{1}{\sqrt{2}}(|k_{s,1} k_{i,1}\rangle + |k_{s,2} k_{i,2}\rangle)$ of two spatial modes, where $k_{s,1} = -k_{i,1}$ and $k_{s,2} = -k_{i,2}$. Under each spatial mode projection, polarization entanglement $|\Psi_{\text{pol}}\rangle = a_p |H_s V_i\rangle + b_p |V_s H_i\rangle$ is present. Consequently, a hyperentangled state $|\Psi_{\text{hyper}}\rangle = |\Psi_{\text{spatial}}\rangle \otimes |\Psi_{\text{pol}}\rangle$ can be generated, as reflected by the simulated density matrices. The predicted fidelity of quantum state produced at $\lambda_p \times 2 = 1562$ nm to the ideal hyperentangled state $|\Psi_{\text{hyper}}\rangle$ yields 98%, indicating the practical feasibility of generating high-quality hyperentanglement. Furthermore, the hyperentanglement can also be optically controlled via pump wavelength through symmetry breaking. A notable advantage of metasurface-generated hyperentanglement is that the number of allowable spatial modes can be >600 times higher than that from bulky crystals (see section S8). This is due to the constraints imposed by longitudinal phase matching conditions in bulky crystals, which limit the biphoton emission range in transverse k space. The use of a small pump beam waist due to a limited aperture of bulky crystals further restricts the spatial bandwidth of each mode.

DISCUSSION

This work uncovers a unique mechanism, by breaking the symmetry of nonlinear polarization, for producing optically tunable quantum entanglement in a nonlinear semiconductor metasurface, ranging from polarization Bell state to hyperentanglement. We show that the number of spatial modes in hyperentanglement can potentially outperform bulky crystals by more than three orders of magnitude. We would like to clarify that the tunability demonstrated in this work is not limited to generating a maximally entangled Bell state, which shows great potential to produce a polarization-entangled state on demand. While Bell states have been widely used in established quantum communication protocols (1), we note that partially entangled states have also found critical applications such as Bell inequality tests (63), quantum teleportation (64), and quantum key distribution (65). Furthermore, this tuning mechanism may unlock a wide range of applications when combined with a pulse-shaped pump containing a frequency comb, such as wavelength-division multiplexing (57, 58), time-division multiplexing (66, 67), ultrafast entanglement switching (22), tunable multiphoton states (54), and more.

Additionally, various methods can work together with adjusting the pump wavelength to deliver even more flexibility. We reveal that the underlying mechanism of tunability is mediated by the nontrivial effect of detuning the biphoton wavelength from the resonance wavelength of the metasurface. This suggests that by integrating phase-change materials or liquid crystals with InGaP metasurfaces, one could dynamically tune the optical resonances and thereby alter the quantum states, which is a new opportunity for future research.

Introducing asymmetric nonlinear responses in quantum flat optics can open directions to tailor on-demand quantum states by engineering the metasurface geometry. This approach builds on the feasibility

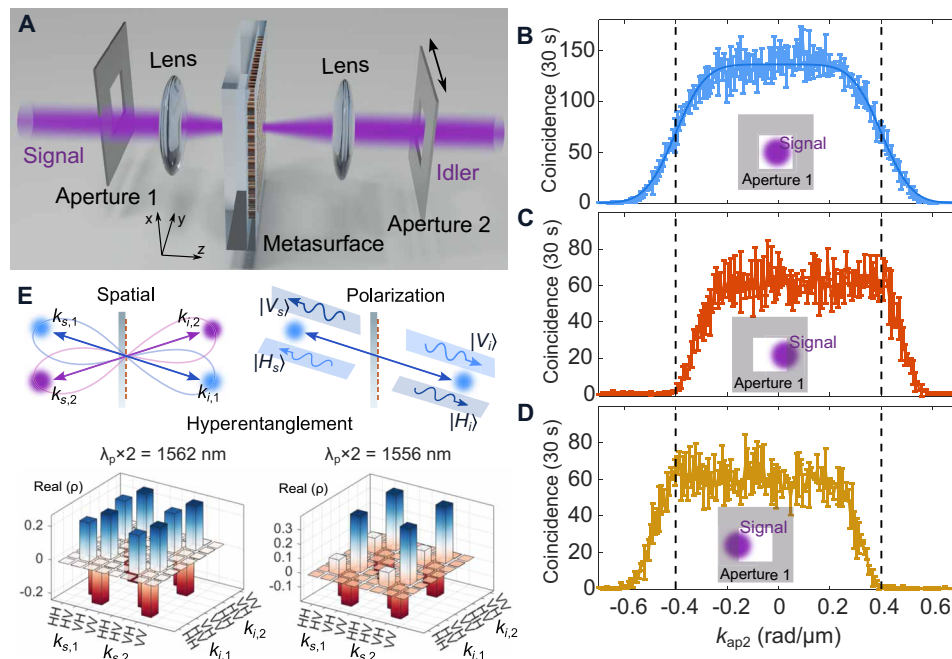


Fig. 4. Perspective of tunable hyperentanglement. (A) Experimental setup for measuring spatial correlations. Aperture 1 is fixed at different positions $k_{ap,s}$, while aperture 2 position $k_{ap,i}$ is scanned through the idler emission along the y axis. The origins of $k_{ap,s}$ and $k_{ap,i}$ are respectively defined as the central position of apertures aligning with the signal/idler emission center. (B to D) Coincidence versus position of aperture 2 $k_{ap,i}$. The position of aperture 1 is set as $k_{ap,s} = 0, -L/2$ and $L/2$, respectively. When the right half of the signal emission is blocked (C), coincidences collected at $k_{ap,i} = L/2$ are closed to the maximum, and almost no idler photons are detected at $k_{ap,i} = -L/2$. Similar behavior is observed when the left half of the signal emission is blocked (D), indicating the anti-spatial correlations of signal and idler photons and the superposition of different spatial modes. The error bars indicate one SD in all plots. (E) Simulated density matrix of hyperentanglement. As shown in the sketch, the photon pairs from the metasurface can manifest spatial ($|\Psi_{\text{spatial}}\rangle = \frac{1}{\sqrt{2}} |k_{s,1}k_{i,1}\rangle + |k_{s,2}k_{i,2}\rangle$) and polarization ($|\Psi_{\text{pol}}\rangle = a_p |H_sV_i\rangle + b_p |V_sH_i\rangle$) entanglements. The simulated density matrix, including both spatial and polarization degrees of freedom, suggests the presence of hyperentanglement, $|\Psi_{\text{hyper}}\rangle = |\Psi_{\text{spatial}}\rangle \otimes |\Psi_{\text{pol}}\rangle$. The hyperentanglement is optically tunable by changing the pump wavelength.

demonstrated in previous studies of classical asymmetric nonlinear processes (31, 32). Leveraging symmetry breaking, the tuning parameter could potentially be extended to include spatial, spectral, and polarization degrees of freedom. Beyond controlling polarization entanglement, this approach may be developed to tailor spatial, spectral, or time-bin entangled states, as well as their hyperentanglement.

Furthermore, our InGaP nanostructures outperform other flat-optics photon-pair sources in many aspects. Their ultrahigh nonlinearity and low fluorescence enable a record-high SPDC rate and CAR in flat-optics quantum light sources at infrared telecommunication wavelengths.

Additionally, this platform may be suited for the monolithic integration of III-V semiconductor lasers, modulators, and detectors on a single chip, leading to ultracompact, robust, and multifunctional quantum photonic devices.

Although the photon-pair rate from the InGaP metasurface is currently lower than that of traditional bulky nonlinear crystals, techniques such as triple resonances at pump, signal, and idler wavelengths are anticipated to boost the SPDC rate substantially. A recent work (68) theoretically predicted a biphoton generation rate of megahertz with a periodically poled triple-resonance metasurface, laying the foundation for future experimental implementations. Additionally, the InGaP metasurface with exceptional control over quantum states can be potentially combined with emerging InGaP integrated photonics platforms [such as microrings (69) or waveguides (70)] with an SPDC

rate outperforming traditional nonlinear material platforms. Combining the unique functionalities demonstrated here, these promising developments position InGaP metasurfaces as attractive candidates for next-generation quantum light sources, offering unprecedented opportunities for quantum information processing.

MATERIALS AND METHODS

Fabrication of the InGaP metasurface

The fabrication steps of the InGaP metasurface are shown in fig. S3. Fabrication begins by unpacking an epi-ready (110) GaAs substrate, on which the InGaP layer is grown epitaxially using metal-organic vapor phase epitaxy (MOCVD). The MOCVD growth is initiated with a surface decontamination step at 730°C under arsine overpressure. The reactor temperature is then reduced to the growth temperature for InGaP growth, where the arsine flow is switched off and the trimethylindium, trimethylgallium, and phosphine flows are switched on. The InGaP composition is calibrated using test samples and x-ray diffraction measurements, and by tuning the ratio of In and Ga precursor flows accordingly. The InGaP growth rate is calibrated using test samples and side-view scanning electron microscopy images from cleaved substrates, and the thickness of 500 nm is achieved by adjusting the growth time. After epitaxy, a SiO₂ layer is deposited and an electron beam resist (ARP6200.09) is spin-coated on the sample. The metasurface pattern is then defined

using electron beam lithography, followed by Cr evaporation and lift-off. The metasurface pattern is transferred first to the SiO₂ layer using dry etching with CHF₃, and subsequently to InGaP using dry etching and SiCl₄. The mask layers are then removed with hydrofluoric acid. The GaAs wafer with the InGaP metasurface is then attached to a quartz substrate using hot embossing with SU8-2 as the interlayer at 250°C and approximately 500 N/cm². Finally, the GaAs wafer is wet etched with phosphoric acid and hydrogen peroxide for approximately 4 hours, and the InGaP metasurface on the quartz is extracted and rinsed in water immediately after it is exposed from underneath the etched GaAs wafer.

Experimental setup for SHG measurement

The experimental setup for SHG characterization is sketched in fig. S4. We focus the fundamental laser beam onto the InGaP metasurface with a near-infrared objective of 20× [numerical aperture (NA) = 0.4] and collect the generated SHG signals with a near-infrared objective of 100× (NA = 0.70). A short pass filter is used to remove the fundamental beam propagating through the metasurface, after which specific polarization of SHG signals is selected with a linear polarization (LP) and the SHG is then measured with an optical spectrometer (Ocean Optics, QE65000). Additionally, a rotational motorized stage (Thorlabs, PRM1/MZ8) with a HWP (Thorlabs, AHWP05M-1600) is added before the metasurface to change the polarization of the fundamental beam, and a wire grid polarizer (LP) (Thorlabs, WP25M-UB) is used after the metasurface to select the polarization of the SHG signals.

Experimental setup for SPDC measurement

The laser (FPL785P, Thorlabs) used for pumping the metasurface has a tunable wavelength range from 779 to 791 nm. A short-pass filter at 850 nm is added before the dichroic mirror to suppress fluorescence co-propagating with the incoming pump beam. The laser is focused onto the metasurface with a lens of 50 mm focal length, and the same lens collimates the signal photons generated from the metasurface. The signal photons are then reflected by the dichroic mirror, after which a long-pass filter at 1400 nm and a band-pass filter at 1570 nm with a 50-nm bandwidth are used to remove the fluorescence from the optics and metasurfaces. In the opposite direction, the idler photons produced from the metasurface are collimated with another lens (focal length of 50 mm), and a set of pass filters with the same specifications as the signal arm is added to filter the pump laser beam and fluorescence from the optics. We include quarter-wave plates (QWPs), HWPs, and polarizers in both signal and idler paths to perform the quantum tomography for the polarization entanglement of signal and idler photons. Photons from both paths are then collected using multimode fibers, which are then directed to single-photon detectors based on InGaAs/InP avalanche photodiodes (ID230, ID Quantique). Timing correlations of the coincidence events are characterized by a time-to-digital converter (ID801, ID Quantique) with a coincidence window set at 0.486 ns.

Supplementary Materials

This PDF file includes:

Sections S1 to S8
Figs. S1 to S17
Table S1
References

REFERENCES AND NOTES

1. S.-K. Liao, W.-Q. Cai, W.-Y. Liu, L. Zhang, Y. Li, J.-G. Ren, J. Yin, Q. Shen, Y. Cao, Z.-P. Li, F.-Z. Li, X.-W. Chen, L.-H. Sun, J.-J. Jia, J.-C. Wu, X.-J. Jiang, J.-F. Wang, Y.-M. Huang, Q. Wang, Y.-L. Zhou, L. Deng, T. Xi, L. Ma, T. Hu, Q. Zhang, Y.-A. Chen, N.-L. Liu, X.-B. Wang, Z.-C. Zhu, C.-Y. Lu, R. Shu, C.-Z. Peng, J.-Y. Wang, J.-W. Pan, Satellite-to-ground quantum key distribution. *Nature* **549**, 43–47 (2017).
2. P.-A. Moreau, E. Toninelli, T. Gregory, M. J. Padgett, Imaging with quantum states of light. *Nat. Rev. Phys.* **1**, 367–380 (2019).
3. S. Slussarenko, G. J. Pryde, Photonic quantum information processing: A concise review. *Appl. Phys. Rev.* **6**, 041303 (2019).
4. T. Stav, A. Faerman, E. Maguid, D. Oren, V. Kleiner, E. Hasman, M. Segev, Quantum entanglement of the spin and orbital angular momentum of photons using metamaterials. *Science* **361**, 1101–1104 (2018).
5. L. Li, Z. Liu, X. Ren, S. Wang, V.-C. Su, M.-K. Chen, C. H. Chu, H. Y. Kuo, B. Liu, W. Zang, G. Guo, L. Zhang, Z. Wang, S. Zhu, D. P. Tsai, Metalens-array-based high-dimensional and multiphoton quantum source. *Science* **368**, 1487–1490 (2020).
6. S. A. Schulz, R. F. Oulton, M. Kenney, A. Alù, I. Staude, A. Bashiri, Z. Fedorova, R. Kolkowski, A. F. Koenderink, X. Xiao, J. Yang, W. J. Peveler, A. W. Clark, G. Perrakis, A. C. Tasolamprou, M. Kafesaki, A. Zaleska, W. Dickson, D. Richards, A. Zayats, H. Ren, Y. Kivshar, S. Maier, X. Chen, M. A. Ansari, Y. Gan, A. Alexeev, T. F. Krauss, A. di Falco, S. D. Gennaro, T. Santiago-Cruz, I. Brener, M. V. Chekhova, R. M. Ma, V. V. Vogler-Neuling, H. C. Weigand, Ü. L. Talts, I. Occhiodori, R. Grange, M. Rahmani, L. Xu, S. M. Kamali, E. Arababi, A. Faraon, A. C. Harwood, S. Vezzoli, R. Sapienza, P. Lalanne, A. Dmitriev, C. Rockstuhl, A. Sprafke, K. Vynck, J. Upham, M. Z. Alam, I. de Leon, R. W. Boyd, W. J. Padilla, J. M. Malof, A. Jana, Z. Yang, R. Colom, Q. Song, P. Genevet, K. Achouri, A. B. Evlyukhin, U. Lemmer, I. Fernandez-Corbaton, Roadmap on photonic metasurfaces. *Appl. Phys. Lett.* **124**, 260701 (2024).
7. A. I. Kuznetsov, M. L. Brongersma, J. Yao, M. K. Chen, U. Levy, D. P. Tsai, N. I. Zheludev, A. Faraon, A. Arbabi, N. Yu, D. Chanda, K. B. Crozier, A. V. Kildishev, H. Wang, J. K. W. Yang, J. G. Valentine, P. Genevet, J. A. Fan, O. D. Miller, A. Majumdar, J. E. Fröch, D. Brady, F. Heide, A. Veeraraghavan, N. Engheta, A. Alù, A. Polman, H. A. Atwater, P. Thureja, R. Paniagua-Dominguez, S. T. Ha, A. I. Barreda, J. A. Schuller, I. Staude, G. Grinblat, Y. Kivshar, S. Peana, S. F. Yelin, A. Senichev, V. M. Shalaev, S. Saha, A. Boltasseva, J. Rho, D. K. Oh, J. Kim, J. Park, R. Devlin, R. A. Pala, Roadmap for optical metasurfaces. *ACS Photonics* **11**, 816–865 (2024).
8. J. Ma, J. Zhang, J. Horder, A. A. Sukhorukov, M. Toth, D. N. Neshev, I. Aharonovich, Engineering quantum light sources with flat optics. *Adv. Mater.* **36**, 2313589 (2024).
9. Q. Guo, X.-Z. Qi, L. Zhang, M. Gao, S. Hu, W. Zhou, W. Zang, X. Zhao, J. Wang, B. Yan, M. Xu, Y.-K. Wu, G. Ede, Z. Xiao, S. A. Yang, H. Gou, Y. P. Feng, G.-C. Guo, W. Zhou, X.-F. Ren, C.-W. Qiu, S. J. Pennycook, A. T. S. Wee, Ultrathin quantum light source with van der Waals NbOCl₂ crystal. *Nature* **613**, 53–59 (2023).
10. T. Santiago-Cruz, S. D. Gennaro, O. Mitrofanov, S. Addamane, J. Reno, I. Brener, M. V. Chekhova, Resonant metasurfaces for generating complex quantum states. *Science* **377**, 991–995 (2022).
11. J. Ma, J. Zhang, Y. Jiang, T. Fan, M. Parry, D. N. Neshev, A. A. Sukhorukov, Polarization engineering of entangled photons from a lithium niobate nonlinear metasurface. *Nano Lett.* **23**, 8091–8098 (2023).
12. W. Jia, G. Saerens, Ü.-L. Talts, H. Weigand, R. J. Chapman, L. Li, R. Grange, Y. Yang, Polarization-entangled Bell state generation from an epsilon-near-zero metasurface. *Sci. Adv.* **11**, eads3576 (2025).
13. J. Noh, T. Santiago-Cruz, V. Sultanov, C. F. Doiron, S. D. Gennaro, M. V. Chekhova, I. Brener, Quantum pair generation in nonlinear metasurfaces with mixed and pure photon polarizations. *Nano Lett.* **24**, 15356–15362 (2024).
14. J. Zhang, J. Ma, M. Parry, M. Cai, R. Camacho-Morales, L. Xu, D. N. Neshev, A. A. Sukhorukov, Spatially entangled photon pairs from lithium niobate nonlocal metasurfaces. *Sci. Adv.* **8**, eabq4240 (2022).
15. J. Ma, J. Ren, J. Zhang, J. Meng, C. McManus-Barrett, K. B. Crozier, A. A. Sukhorukov, Quantum imaging using spatially entangled photon pairs from a nonlinear metasurface. *eLight* **5**, 2 (2025).
16. V. Sultanov, A. Kavčić, E. Kokkinakis, N. Sebastián, M. V. Chekhova, M. Humar, Tunable entangled photon-pair generation in a liquid crystal. *Nature* **631**, 294–299 (2024).
17. V. Sultanov, T. Santiago-Cruz, M. V. Chekhova, Flat-optics generation of broadband photon pairs with tunable polarization entanglement. *Opt. Lett.* **47**, 3872–3875 (2022).
18. M. A. Weissflog, A. Fedotova, Y. L. Tang, E. A. Santos, B. Laudert, S. Shinde, F. Abtahi, M. Afsharnia, I. Pérez, P. Pérez, S. Ritter, H. Qin, J. Janousek, S. Shradha, I. Staude, S. Saravi, T. Pertsch, F. Setzpfandt, Y. R. Lu, F. Eilenberger, A tunable transition metal dichalcogenide entangled photon-pair source. *Nat. Commun.* **15**, 7600 (2024).
19. J. Feng, Y.-K. Wu, R. Duan, J. Wang, W. Chen, J. Qin, Z. Liu, G.-C. Guo, X.-F. Ren, C.-W. Qiu, Polarization-entangled photon-pair source with van Der Waals 3R-WS₂ Crystal. *eLight* **4**, 16 (2024).

20. H. Liang, T. Gu, Y. Lou, C. Yang, C. Ma, J. Qi, A. A. Bettiol, X. Wang, Tunable polarization entangled photon-pair source in rhombohedral boron nitride. *Sci. Adv.* **11**, eadt3710 (2025).
21. X. Lyu, L. Kallioniemi, H. Hong, R. Qu, Y. Zhang, J. Zúñiga-Perez, K. Liu, W. Gao, A tunable entangled photon-pair source based on a van der Waals insulator. *Nat. Commun.* **16**, 1899 (2025).
22. J. M. Donohue, J. Lavoie, K. J. Resch, Ultrafast time-division demultiplexing of polarization-entangled photons. *Phys. Rev. Lett.* **113**, 163602 (2014).
23. A. Kawasaki, H. Brunel, R. Ide, T. Suzuki, T. Kashiwazaki, A. Inoue, T. Umeki, T. Yamashima, A. Sakaguchi, K. Takase, M. Endo, W. Asavanant, A. Furusawa, Real-time observation of picosecond-timescale optical quantum entanglement towards ultrafast quantum information processing. *Nat. Photonics* **19**, 271–276 (2025).
24. L. H. Nicholls, F. J. Rodríguez-Fortuño, M. E. Nasir, R. M. Córdova-Castro, N. Olivier, G. A. Wurtz, A. V. Zayats, Ultrafast synthesis and switching of light polarization in nonlinear anisotropic metamaterials. *Nat. Photonics* **11**, 628–633 (2017).
25. L. Fan, J. Wang, L. T. Varghese, H. Shen, B. Niu, Y. Xuan, A. M. Weiner, M. Qi, An all-silicon passive optical diode. *Science* **335**, 447–450 (2012).
26. D. L. Sounas, A. Alù, Non-reciprocal photonics based on time modulation. *Nat. Photonics* **11**, 774–783 (2017).
27. L. D. Tzuang, K. Fang, P. Nussenzeig, S. Fan, M. Lipson, Non-reciprocal phase shift induced by an effective magnetic flux for light. *Nat. Photonics* **8**, 701–705 (2014).
28. Z. Yu, S. Fan, Complete optical isolation created by indirect interband photonic transitions. *Nat. Photonics* **3**, 91–94 (2009).
29. M. Cotrufo, A. Cordaro, D. L. Sounas, A. Polman, A. Alù, Passive bias-free non-reciprocal metasurfaces based on thermally nonlinear quasi-bound states in the continuum. *Nat. Photonics* **18**, 81–90 (2024).
30. A. Tripathi, C. F. Ugwu, V. S. Asadchy, I. Faniaye, I. Kravchenko, S. Fan, Y. Kivshar, J. Valentine, S. S. Kruk, Nanoscale optical nonreciprocity with nonlinear metasurfaces. *Nat. Commun.* **15**, 5077 (2024).
31. S. Boroviks, A. Kiselev, K. Achouri, O. J. F. Martin, Demonstration of a plasmonic nonlinear pseudodiode. *Nano Lett.* **23**, 3362–3368 (2023).
32. S. S. Kruk, L. Wang, B. Sain, Z. Dong, J. Yang, T. Zentgraf, Y. Kivshar, Asymmetric parametric generation of images with nonlinear dielectric metasurfaces. *Nat. Photonics* **16**, 561–565 (2022).
33. N. Shitrit, J. Kim, D. S. Barth, H. Ramezani, Y. Wang, X. Zhang, Asymmetric free-space light transport at nonlinear metasurfaces. *Phys. Rev. Lett.* **121**, 046101 (2018).
34. H. Tang, Y. Wang, X. Ni, K. Watanabe, T. Taniguchi, P. Jarillo-Herrero, S. Fan, E. Mazur, A. Yacoby, Y. Cao, On-chip multi-degree-of-freedom control of two-dimensional materials. *Nature* **632**, 1038–1044 (2024).
35. R. Huang, A. Miranowicz, J. Q. Liao, F. Nori, H. Jing, Nonreciprocal photon blockade. *Phys. Rev. Lett.* **121**, 153601 (2018).
36. Y.-F. Jiao, S.-D. Zhang, Y.-L. Zhang, A. Miranowicz, L.-M. Kuang, H. Jing, Nonreciprocal optomechanical entanglement against backscattering losses. *Phys. Rev. Lett.* **125**, 143605 (2020).
37. M.-X. Dong, K.-Y. Xia, W.-H. Zhang, Y.-C. Yu, Y.-H. Ye, E.-Z. Li, L. Zeng, D.-S. Ding, B.-S. Shi, G.-C. Guo, F. Nori, All-optical reversible single-photon isolation at room temperature. *Sci. Adv.* **7**, eabe8924 (2021).
38. S. Zhang, Y. Hu, G. Lin, Y. Niu, K. Xia, J. Gong, S. Gong, Thermal-motion-induced non-reciprocal quantum optical system. *Nat. Photonics* **12**, 744–748 (2018).
39. Q. Bin, H. Jing, Y. Wu, F. Nori, X.-Y. Lü, Nonreciprocal bundle emissions of quantum entangled pairs. *Phys. Rev. Lett.* **133**, 043601 (2024).
40. G.-L. Zhu, C.-S. Hu, H. Wang, W. Qin, X.-Y. Lü, F. Nori, Nonreciprocal superradiant phase transitions and multicriticality in a cavity QED system. *Phys. Rev. Lett.* **132**, 193602 (2024).
41. A. Graf, S. D. Rogers, J. Staffa, U. A. Javid, D. H. Griffith, Q. Lin, Nonreciprocity in photon pair correlations of classically reciprocal systems. *Phys. Rev. Lett.* **128**, 213605 (2022).
42. Y. Ueno, V. Ricci, G. I. Stegeman, Second-order susceptibility of Ga_{0.5}In_{0.5}P Crystals at 1.5 μm and their feasibility for waveguide quasi-phase matching. *J. Opt. Soc. Am. B* **14**, 1428–1436 (1997).
43. C. Son, V. Sultanov, T. Santiago-Cruz, A. P. Anthur, H. Zhang, R. Paniagua-Dominguez, L. Krivitsky, A. I. Kuznetsov, M. V. Chekhova, Photon pairs bi-directionally emitted from a resonant metasurface. *Nanoscale* **15**, 2567–2572 (2023).
44. S. Liu, G. A. Keeler, J. L. Reno, M. B. Sinclair, I. Brener, III–V Semiconductor nanoresonators—A new strategy for passive, active, and nonlinear all-dielectric metamaterials. *Adv. Opt. Mater.* **4**, 1457–1462 (2016).
45. M. R. Shcherbakov, S. Liu, V. V. Zubyuk, A. Vaskin, P. P. Vabishchevich, G. Keeler, T. Pertsch, T. V. Dolgova, I. Staude, I. Brener, A. A. Fedyanin, Ultrafast all-optical tuning of direct-gap semiconductor metasurfaces. *Nat. Commun.* **8**, 17 (2017).
46. G. Marino, A. S. Solntsev, L. Xu, V. F. Gili, L. Carletti, A. N. Poddubny, M. Rahmani, D. A. Smirnova, H. Chen, A. Lematre, G. Zhang, A. V. Zayats, C. D. E. Angelis, G. Leo, A. A. Sukhorukov, D. N. Neshev, Spontaneous photon-pair generation from a dielectric nanoantenna. *Optica* **6**, 1416 (2019).
47. M. Parry, A. Mazzanti, A. Poddubny, G. Della Valle, D. N. Neshev, A. A. Sukhorukov, Enhanced generation of nondegenerate photon pairs in nonlinear metasurfaces. *Adv. Photonics* **3**, 055001 (2021).
48. T. Santiago-Cruz, A. Fedotova, V. Sultanov, M. A. Weissflog, D. Arslan, M. Younesi, T. Pertsch, I. Staude, F. Setzpfandt, M. Chekhova, Photon pairs from resonant metasurfaces. *Nano Lett.* **21**, 4423–4429 (2021).
49. R. B. Jin, R. Shimizu, K. Wakui, M. Fujiwara, T. Yamashita, S. Miki, H. Terai, Z. Wang, M. Sasaki, Pulsed sagnac polarization-entangled photon source with a PPKTP crystal at telecom wavelength. *Opt. Express* **22**, 11498–11507 (2014).
50. J. F. Clauser, A. Shimony, Bell's theorem. Experimental tests and implications. *Rep. Prog. Phys.* **41**, 1881–1927 (1978).
51. D. F. V. James, P. G. Kwiat, W. J. Munro, A. G. White, Measurement of qubits. *Phys. Rev. A* **64**, 052312 (2001).
52. M. Parry, K. B. Crozier, A. A. Sukhorukov, D. N. Neshev, Optimization of metasurfaces for lasing with symmetry constraints on the modes. *Phys. Rev. B* **109**, 075406 (2024).
53. V. Borshch, S. V. Shiyankovskii, O. D. Lavrentovich, Nanosecond electro-optic switching of a liquid crystal. *Phys. Rev. Lett.* **111**, 107802 (2013).
54. C. Reimer, M. Kues, P. Roztock, B. Wetzel, F. Grazioso, B. E. Little, S. T. Chu, T. Johnston, Y. Bromberg, L. Caspani, D. J. Moss, R. Morandotti, Generation of multiphoton entangled quantum states by means of integrated frequency combs. *Science* **351**, 1176–1180 (2016).
55. A. L. Gaeta, M. Lipson, T. J. Kippenberg, Photonic-chip-based frequency combs. *Nat. Photonics* **13**, 158–169 (2019).
56. A. Pasquazi, M. Peccianti, L. Razzari, D. J. Moss, S. Coen, M. Erkintalo, Y. K. Chembo, T. Hansson, S. Wabnitz, P. Del'Haye, X. Xue, A. M. Weiner, R. Morandotti, Micro-combs: A novel generation of optical sources. *Phys. Rep.* **729**, 1–81 (2018).
57. S. Wengerowsky, K. K. Joshi, F. Steinlechner, H. Hübel, R. Ursin, An entanglement-based wavelength-multiplexed quantum communication network. *Nature* **564**, 225–228 (2018).
58. I. Herbauts, B. Blauensteiner, A. Poppe, T. Jennewein, H. Hübel, Demonstration of active routing of entanglement in a multi-user network. *Opt. Express* **21**, 29013 (2013).
59. M. A. Hall, J. B. Altepeter, P. Kumar, Ultrafast switching of photonic entanglement. *Phys. Rev. Lett.* **106**, 053901 (2011).
60. J. Roslund, R. M. De Araújo, S. Jiang, C. Fabre, N. Treps, Wavelength-multiplexed quantum networks with ultrafast frequency combs. *Nat. Photonics* **8**, 109–112 (2014).
61. O. Pinel, P. Jian, R. M. De Araújo, J. Feng, B. Chalopin, C. Fabre, N. Treps, Generation and characterization of multimode quantum frequency combs. *Phys. Rev. Lett.* **108**, 083601 (2012).
62. F. Setzpfandt, A. S. Solntsev, J. Titchener, C. W. Wu, C. Xiong, R. Schiek, T. Pertsch, D. N. Neshev, A. A. Sukhorukov, Tunable generation of entangled photons in a nonlinear directional coupler. *Laser Photonics Rev.* **10**, 131–136 (2016).
63. M. Giustina, M. A. M. Versteegh, S. Wengerowsky, J. Handsteiner, A. Hochrainer, K. Phelan, F. Steinlechner, J. Kofler, J. Å. Larsson, C. Abellán, W. Amaya, V. Pruneri, M. W. Mitchell, J. Beyer, T. Gerrits, A. E. Lita, L. K. Shalm, S. W. Nam, T. Scheidl, R. Ursin, B. Wittmann, A. Zeilinger, Significant-loophole-free test of Bell's theorem with entangled photons. *Phys. Rev. Lett.* **115**, 250401 (2015).
64. J. Modlowska, A. Grudka, Nonmaximally entangled states can be better for multiple linear optical teleportation. *Phys. Rev. Lett.* **100**, 110503 (2008).
65. P. Xue, C.-F. Li, G.-C. Guo, Efficient quantum-key-distribution scheme with nonmaximally entangled states. *Phys. Rev. A* **64**, 032305 (2001).
66. Y.-L. Tang, H.-L. Yin, Q. Zhao, H. Liu, X.-X. Sun, M.-Q. Huang, W.-J. Zhang, S.-J. Chen, L. Zhang, L.-X. You, Z. Wang, Y. Liu, C.-Y. Lu, X. Jiang, X. Ma, Q. Zhang, T.-Y. Chen, J.-W. Pan, Measurement-device-independent quantum key distribution over untrusted metropolitan network. *Phys. Rev. X* **6**, 011024 (2016).
67. B. Fröhlich, J. F. Dynes, M. Lucamarini, A. W. Sharpe, Z. Yuan, A. J. Shields, A quantum access network. *Nature* **501**, 69–72 (2013).
68. J. Zhang, C. Shi, J. Ma, F. Setzpfandt, T. Pertsch, C. Bao, J. Zhang, A. A. Sukhorukov, Broadband bright biphotons from periodically poled triple-resonance metasurface. *arXiv:2502.08990* [physics.optics] (2025).
69. M. Zhao, K. Fang, InGaP quantum nanophotonic integrated circuits with 1.5% nonlinearity-to-loss ratio. *Optica* **9**, 258 (2022).
70. J. Akin, Y. L. Zhao, Y. Misra, A. K. M. N. Haque, K. J. Fang, InGaP $\chi^{(2)}$ integrated photonics platform for broadband, ultra-efficient nonlinear conversion and entangled photon generation. *Light Sci. Appl.* **13**, 290 (2024).
71. R. W. Boyd, *Nonlinear Optics* (Academic Press, ed. 4, 2020).
72. R. W. Boyd, A. L. Gaeta, E. Giese, "Nonlinear optics" in *Springer Handbook of Atomic, Molecular, and Optical Physics* (Springer, 2008), pp. 1097–1110.
73. C. Okoth, A. Cavanna, T. Santiago-Cruz, M. V. Chekhova, Microscale generation of entangled photons without momentum conservation. *Phys. Rev. Lett.* **123**, 263602 (2019).
74. A. L. Shelankov, G. E. Pikus, Reciprocity in reflection and transmission of light. *Phys. Rev. B* **46**, 3326–3336 (1992).
75. D. J. Willcock, *Molecular Symmetry* (John Wiley & Sons, 2009).
76. K. Sakoda, *Optical Properties of Photonic Crystals* (Springer, 2004).

77. R. McWeeny, *Symmetry: An Introduction to Group Theory and Its Applications* (Pergamon Press, 1963).
78. M. B. Parry, Projection operators for MATLAB (2023). https://github.com/mettw/Projection_Operators.
79. J. Fraleigh, R. Beauregard, *Linear Algebra* (Addison-Wesley, 1987).
80. W. E. Brittin, A. Y. Sakakura, Projection operator techniques in physics. *J. Math. Phys.* **25**, 1274–1295 (1984).
81. C. E. Kuklewicz, M. Fiorentino, G. Messin, F. N. C. Wong, J. H. Shapiro, High-flux source of polarization-entangled photons from a periodically poled KTiOPO₄ parametric down-converter. *Phys. Rev. A* **69**, 013807 (2004).
82. A. V. Burlakov, M. V. Chekhova, O. A. Karabutova, D. N. Klyshko, S. P. Kulik, Polarization state of a biphoton: Quantum ternary logic. *Phys. Rev. A* **60**, R4209–R4212 (1999).
83. Kwiat Quantum Information Group, Quantum Tomography. <https://quantumtomo.web.illinois.edu/>.
84. G. M. D'Ariano, M. G. Paris, M. F. Sacchi, Quantum tomography. *Adv. Imaging Electron Phys.* **128**, 205–308 (2003).
85. W. K. Wootters, Entanglement of formation of an arbitrary state of two qubits. *Phys. Rev. Lett.* **80**, 2245–2248 (1998).
86. L. Huang, K. Xu, D. Yuan, J. Hu, X. Wang, S. Xu, Sub-wavelength patterned pulse laser lithography for efficient fabrication of large-area metasurfaces. *Nat. Commun.* **13**, 5823 (2022).
87. A. She, S. Zhang, S. Shian, D. R. Clarke, F. Capasso, Large area metalenses: Design, characterization, and mass manufacturing. *Opt. Express* **26**, 1573–1585 (2018).
88. I. Kviatkovsky, H. M. Chrzanowski, E. G. Avery, H. Bartolomaeus, S. Ramelow, Microscopy with undetected photons in the mid-infrared. *Sci. Adv.* **6**, eabd0264 (2020).
89. P. A. Moreau, E. Toninelli, P. A. Morris, R. S. Aspden, T. Gregory, G. Spalding, R. W. Boyd, M. J. Padgett, Resolution limits of quantum ghost imaging. *Opt. Express* **26**, 7528 (2018).

Acknowledgments: We thank S. Klimmer for building the automated setup for SHG measurements. **Funding:** This work was supported by the Australian Research Council (DP190101559, CE200100010) and Meta Active IRTG 2675 (437527638). Metasurface fabrication was performed at the Australian National University node of the Australian National Fabrication Facility (ANFF), a company established under the National Collaborative Research Infrastructure Strategy to provide nano- and microfabrication facilities for Australian researchers. **Author contributions:** A.A.S. and J.M. conceived the idea, designed the research, and supervised the project. J.M., T.F., S.S., C.M.-B., and J.Z. performed the quantum characterization and processed the data. R.C.M. L.V.M., and D.N.N. conducted the classical nonlinear experiments. T.H. designed the materials aspects of the project and developed and optimized the epitaxy of InGaP [110] crystals, as well as the fabrication process of the metasurface. H.H.T. and C.J. supervised the material development and fabrication. T.F., J.M., M.P., and A.A.S. performed the theoretical studies. A.A.S., D.N.N., F.S., J.M., and T.F. analyzed and discussed the results. J.M. wrote the paper with input from all authors. **Competing interests:** The authors declare that they have no competing interests. **Data and materials availability:** All data needed to evaluate the conclusions in the paper are present in the paper and/or the Supplementary Materials.

Submitted 7 November 2024

Accepted 3 June 2025

Published 9 July 2025

10.1126/sciadv.adu4133